I&EC research
Industrial & Engineering Chemistry Research

pubs.acs.org/IECR

Article

# Flow Pattern and Mixing Characteristics of Highly Viscous Fluids in a Dynamic Mixer

Junhao Wang, Zhipeng Li,* Zhengming Gao,* and J. J. Derksen

Cite This: *Ind. Eng. Chem. Res.* 2024, 63, 4164−4175

Read Online

ACCESS | Metrics & More | Article Recommendations

**ABSTRACT:** Computational fluid dynamics (CFD) was used to assess the flow patterns and mixing characteristics of highly viscous fluids in a dynamic mixer. The simulated concentration distribution was validated by the data measured using planar laser-induced fluorescence (PLIF). The refractive indices of the two fluids and the transparent solid material comprising the mixer were matched to minimize the bending of sent and received light. The simulated concentration fields agreed well with the measured concentration fields. The flow pattern and mixing performance were quantitatively evaluated by using the mixing index $\lambda$ and the coefficient of variation (COV), respectively. After the mixing performance reached time independence, a reduction of the COV at the outlet was associated with a slight increase of the volume-averaged $|\lambda|$. The results suggested that elongational flow was more effective than shear flow in obtaining a more uniform concentration distribution in highly viscous fluids.

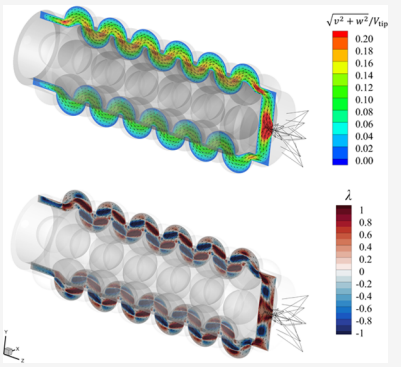




## 1. INTRODUCTION

Polymer industrial applications often require the blending of highly viscous fluids. Mixing in highly viscous systems predominantly takes place under laminar conditions. The effect of laminar mixing is key to determining the quality of the polymer composites. However, the mixing process of a highly viscous fluid with a viscosity of over 10 Pa·s is a formidable task. On the one hand, the laminar mixing pattern lacks turbulent eddies to assist species transport; on the other hand, low diffusion coefficients of highly viscous fluids with orders of magnitude around $10^{-11}$ $m^2/s$ and even lower strongly limit diffusive mixing.[1]

Attempts to overcome these challenges have led to the development of mixing strategies that impose deformation on highly viscous fluids, including shear, stretching, folding, and reorientation.[2] These have been enforced by the rotor against the vessel wall[3] or stator.[4] The cavity transfer mixer (CTM), a dynamic mixer variant, was devised by Gale to enhance the mixing performance of polymers.[5] The CTM includes the rotor and the stator, both with a series of hemispherical cavities, as illustrated in Figure 1. Rotor rotation causes a continuous change in the relative location of the fluid within the cavities. Simultaneously, there is a pressure-driven through-flow in the CTM. The flow field induces lateral and transverse fluid motions involving pulling, shearing, compression, folding, and reorientation by the moving geometry and pressure load.

Effective design and optimization of CTM devices demand a thorough understanding of the flow patterns and associated mixing characteristics. To demonstrate the potential of the CTM for enhanced mixing, researchers, including Wang and Manas-Zloczower,[6] utilized computational fluid dynamics (CFD) simulations to analyze the three-dimensional flow field within the CTM, leading to discussions on its potential for dispersive mixing in their report. Grosso et al.[7] performed a thorough numerical study to discuss the mixing performance within the CTM. A finite element solver and a mapping method were implemented to predict the concentration field. Their study underscored the significant impact of factors, such as the geometric dimensions of cavities and an optimal ratio, defined as the axial and tangential velocity of the fluid, on the mixing performance of the CTM. Huang et al.[8] simulated the mixing process of Newtonian viscous fluids, assessing how the clearance between the rotor and stator influences mixing performance. Their findings suggested that a smaller gap improves mixing but results in higher energy consumption.

The quantitative visualization of the highly viscous fluid flow and mixing involves the application of laser-based flow diagnostic methods. These techniques enable the measurement of the mixing performance by examining the interplay between the flow field and fluid rheology. The particle image velocimetry (PIV) technique was used by Jaffer et al.[9] to measure the flow fields inside the twin-screw extruder. The PIV experimental data were used to validate the simulated flow

**Received:** December 22, 2023
**Revised:** January 31, 2024
**Accepted:** February 9, 2024
**Published:** February 26, 2024





https://doi.org/10.1021/acs.iecr.3c04570
*Ind. Eng. Chem. Res.* 2024, 63, 4164−4175

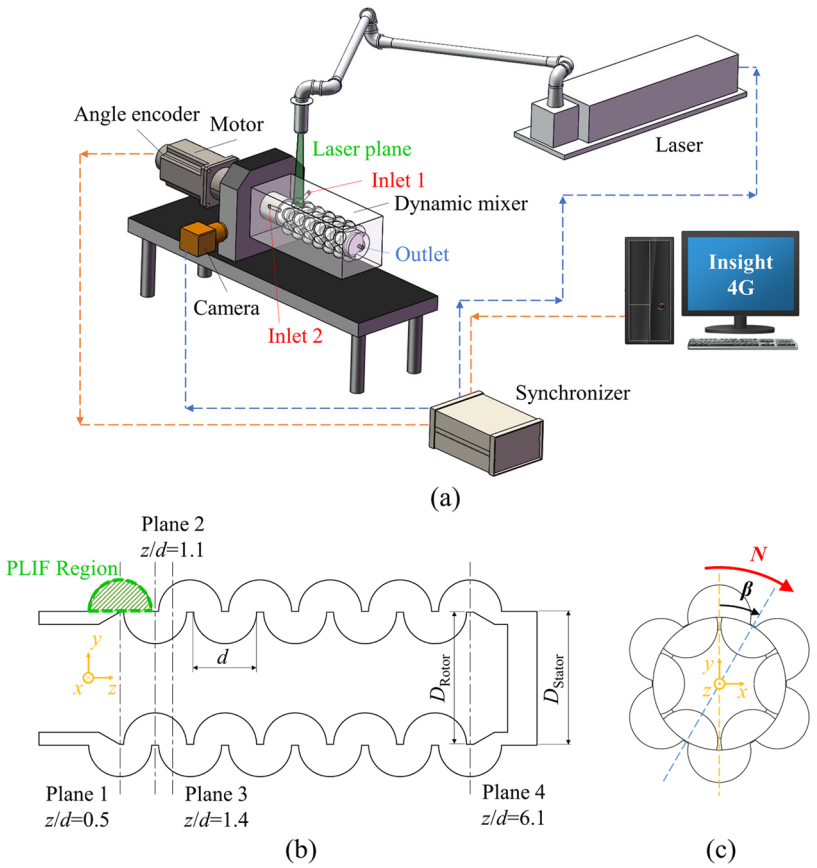


**Figure 1.** (a) PLIF experimental setup: there are six rows of stator cavities and five rows of rotor cavities in a three-dimensional dynamic mixer. (b) Four planes perpendicular to the $z$-direction, where we mainly show the results and the PLIF measurement region. (c) Definition of angle $\beta$ between the stator and rotor.

data at different flow rates, and they were in good agreement at high flow rates. These results show the feasibility of implementing optical measurements in this highly complex geometry. Cortada-Garcia et al.[10] obtained velocity profiles in a laboratory-scale stirred tank filled with highly viscous shear-thinning fluids. PIV experiments were evaluated in their study, and the interrogation error was identified as the most significant error. Alberini et al.[11] used planar laser-induced fluorescence (PLIF) to examine the mixing performance of KM static mixers with highly viscous fluids. They observed that when a high-viscosity liquid is mixed with a low-viscosity continuous phase, a high-viscosity fluid filament is transformed into a point, a phenomenon that has not been detected by conventional methods.

Optical experiments on mixing (including PLIF) in dynamic and complex geometries with strongly curved walls need further investigation. The challenge in this work is how to fulfill the refractive index matching (RIM) of both working fluids and working fluids with the transparent solid material of the mixer to allow for unobstructed optical access.[12,13] PLIF images can not only display the mixing effectiveness of highly viscous fluids in the dynamic mixer at specific conditions but also validate simulations. Through this technique, the understanding of mixing quality has moved from an empirical one, relying on a single parameter, to a multidimensional one, incorporating a number of factors.[11]

This paper extends our earlier research on mixing highly viscous fluids in dynamic mixers.[8] Unlike the previous paper that used PIV experiments for validation, our current study presents scalar concentration distribution data measured with PLIF, providing a direct demonstration of scalar mixing. In earlier studies conducted within the dynamic mixer, the focus was on exploring the influence of buoyancy, originating from fluids with different densities, on the mixing performance. A dimensionless number, $Ar/Re$, calculated as the ratio of buoyancy ($\Delta\rho g L^3$) to viscous force $\left(\mu\frac{U}{L}L^2\right)$, was introduced to describe the mixing efficiency of miscible Newtonian fluids with density differences. The conclusion was drawn that mixing processes with identical $Ar/Re$ values are essentially similar, and the greater the $Ar/Re$, the poorer the mixing performance.

In this work, the first purpose is to showcase the applicability of using PLIF experiments in such structurally complex environments with strongly curved walls and relative motion between components. Then, the simulation results and numerical method are validated by comparing the experimental results with the simulated data. Third, this study explores the correlation between the flow patterns and mixing performance for highly viscous fluids.

This paper follows the structure outlined below, and the next section introduces the flow system and the PLIF experimental setup. Following that, we provide a concise summary of the numerical approaches employed, referencing the relevant literature. The results section begins by validating simulations using PLIF experimental data. Next, we study the flow patterns within the dynamic mixer. The mixing index $\lambda$ was chosen to evaluate the levels of elongational flow and shearing flow


https://doi.org/10.1021/acs.iecr.3c04570
Ind. Eng. Chem. Res. 2024, 63, 4164−4175

quantitatively. Then, under different operating conditions, we systematically analyzed the effect of the mixing performance on the flow pattern. We attempted to relate the mixing performance to $\lambda$. The concluding section summarizes the key findings and discusses avenues for future research.

## 2. FLOW SYSTEM

The dynamic mixer, whose layout is depicted in Figure 1(a), is constructed from poly(methyl methacrylate) (PMMA). Agitation is achieved by cavities in the rotor and stator. In the axial direction ($z$-direction), there are five rows of cavities on the rotor and six rows of cavities on the stator. There are six rows of cavities on the circumference of the rotor and stator. There are two inlets and one outlet connected to the stator through holes with a diameter of 10 mm. The two inlets are symmetrically positioned along the $x/d$ = 0 plane and are situated on the left side of the dynamic mixer, while the outlet is located at the center on the right side of the dynamic mixer. The working fluids are fed by two external gear pumps (Cixi, China) connected to the two inlets. The flow rate is determined by a preliminary calibration. Volumetric flow rates of 64 and 16 mL/min exist at inlets 1 and 2, respectively. Initially, the dynamic mixer contained liquid 1, with inlet 1 filled with fluid 1 and inlet 2 filled with fluid 2. The rotor had a diameter of 84 mm, and the stator had a diameter of 85 mm. The cavities of the rotor and stator have a diameter of 40 mm.

Computer-controlled stepping motors enforce the rotor at $N$ = 1 rev/min (CNYOHO, China). The rotor and stator positions are synchronized by an angle encoder that generates transistor−transistor logic (TTL) signals. The relative position between the rotor and stator is represented by the angle $\beta$, as shown in the Figure 1(c).

The experiment temperature was kept at 21 ± 0.5 °C. The experimental study utilized a maltose aqueous solution (94.4 wt %) as both working fluids 1 and 2. The solution had a density $\rho$ = 1386 kg/m$^3$, viscosity $\mu$ = 20 Pa·s, and refractive index $n$ = 1.487 at 21 °C. The viscosity and refractive index were measured at a constant temperature of 21 °C, using a MARS40 Rheometer (Haake, Germany) and a WAY-2W Abbe refractometer (INESA, China), respectively. The optical distortion was minimized by matching the refractive index of this solution to that of PMMA ($n$ = 1.487 at 21 °C).

In this experimental study, the Reynolds number is defined as $Re = \frac{\rho N D_{\text{Rotor}}^2}{\mu} = 0.002$ indicating a laminar flow. The Schmidt number $Sc = \frac{\mu}{\rho D_m}$ is considered a critical parameter to evaluate the mixing efficiency of the miscible highly viscous fluids. Based on the experimental data of Zhu et al.[14] for maltose aqueous solutions, the diffusion coefficient $D_m$ was determined to be $1 \times 10^{-11}$ m$^2$/s. In this study, the Schmidt number was calculated as $1.4 \times 10^9$. The Peclet number $Pe = ScRe = \frac{N D_{\text{rotor}}^2}{D_m}$, a parameter indicating whether mass transfer is governed by diffusion or convection, significantly surpasses 1 in our study. Consequently, both Schmidt and Peclet numbers were well above 1, indicating that the mixing in this study is mainly controlled by reducing the scale of segregation through convective processes, after which diffusion over very short distances (see Section 5.1) completes homogenization.

## 3. PLIF EXPERIMENTAL SETUP

For the PLIF measurements, we employed a dual-pulse laser system (200 mJ Nd: YGA, Beamtech, China) operating at a wavelength of 532 nm. The optical setup included a high-resolution CMOS camera (5120 × 5120 pixels, TSI) equipped with an optical filter and synchronized using a dedicated synchronizer (TSI). Laser control, synchronization between the laser and camera, and data acquisition were managed with Insight 4G software (TSI). To visualize the flow, the laser light was directed vertically into the cavity through the lateral wall of the dynamic mixer, as illustrated in Figure 1(a),(b).

For the PLIF measurements, rhodamine B served as a tracer in fluid 2 at a concentration of 50 $\mu$g·L$^{-1}$. Rhodamine B has absorption and maximum emission wavelengths of 532 and 590 nm, respectively.[15] To selectively capture the excited fluorescence, a precise, sharp cutoff filter was positioned in front of the camera, obstructing light with wavelengths less than 550 nm. The exposure time of the CMOS camera was set at 2 ms. The shooting frequency and the time interval between adjacent laser pulses were both regulated by an angle encoder.

To obtain the absolute value of concentration, the tracer concentration $C$ and the fluorescence intensity $F$ must be calibrated. Their relationship is[16]

$$F \propto \frac{I}{1 + I/I_{\text{sat}}} C \tag{1}$$

where $I_{\text{sat}}$ is the saturation intensity of the colorant. Since $I \ll I_{\text{sat}}$, eq 1 will be converted to

$$F \propto IC \tag{2}$$

Figure 2 depicts the fluorescence intensity at the measurement plane as a function of the rhodamine B concentration,

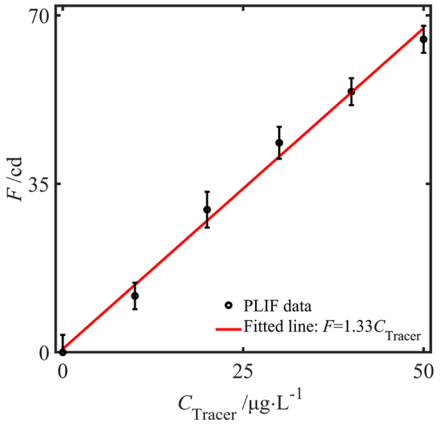


**Figure 2.** Fluorescence intensity of rhodamine B plotted against the tracer concentration in the working fluid at 21 °C. The error bar, denoting one standard deviation, reveals an uncertainty of 0.059 with a coefficient of 1.33.

ranging from 0 to 50 $\mu$g·L$^{-1}$. This representation reveals a clearly established linear correlation. Consequently, the camera-recorded fluorescence intensity provides a direct indicator of the concentration of fluid containing rhodamine B (fluid 2).

## 4. SIMULATION

**4.1. Governing Equations.** The conservation of mass and the momentum for Newtonian fluid are described by the continuity equation and Navier−Stokes equation as follows



https://doi.org/10.1021/acs.iecr.3c04570
Ind. Eng. Chem. Res. 2024, 63, 4164−4175

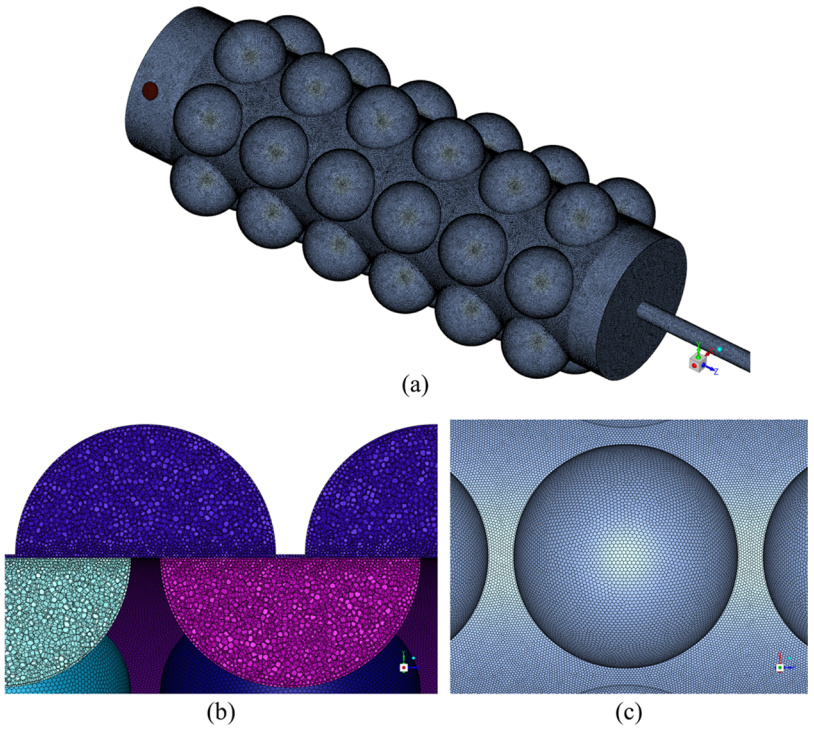


**Figure 3.** Polyhedral mesh for the simulation: (a) the surface grid of the dynamic mixer; (b) the volume grid in the cavities; and (c) the grid on the surface of the cavity.

$$\nabla \cdot \boldsymbol{V} = 0 \tag{3}$$

$$\frac{\partial \boldsymbol{V}}{\partial t} + \boldsymbol{V} \cdot \nabla \boldsymbol{V} = -\frac{\nabla p}{\rho} + \nabla \cdot \left[ \frac{\mu}{\rho} (\nabla \boldsymbol{V} + \nabla \boldsymbol{V}^T) \right] + g \tag{4}$$

where $\rho$ is the density, $V$ is the velocity, $p$ is the pressure, and $g$ is the acceleration due to gravity, which is assigned a value of 9.81 m/s$^2$ in the negative y direction.

The simulation of two miscible, highly viscous fluids mixed in a dynamic mixer uses a species transport model. The conservation equation for fluid 1, obtained by Irani and Adamson,[17] is given by

$$\frac{\partial C_1}{\partial t} + \boldsymbol{V} \cdot \nabla C_1 = \nabla \cdot (D \nabla C_1) \tag{5}$$

where $C_1$ is the mass fraction of fluid 1. The mass fraction of fluid 2 is given by

$$C_2 = 1 - C_1 \tag{6}$$

**4.2. Numerical Details.** In this study, the geometrical configuration utilized in the CFD simulations was the same as that employed in PLIF experiments. Polyhedral cells were created utilizing the commercial software Fluent Meshing, as shown in Figure 3. In comparison to tetrahedral cells, polyhedral cells offer clear advantages in computational efficiency and precision.[18] We conducted thorough grid independent studies, the results of which are presented in the next section.

As this simulation focuses on laminar incompressible flows, Ansys Fluent software was employed with a pressure-based solver. The simulation of rotor motion employed the sliding mesh technique. The spatial discretization for species conservation equations used the third-order MUSCL scheme.[19] Coupling pressure and velocity were achieved through the SIMPLE algorithm. A second-order implicit scheme was used for time advancement. All wall boundaries were maintained under a no-slip condition. To ensure a Courant−Friedrichs−Levy number below 1 for varying angular velocities,[20] the time step $\Delta t$ was varied from 0.1 to 0.025 s. Simulations were performed on a high-performance computer equipped with two Intel Xeon Gold 6240 CPUs and 128 GB memory. The case with 4 million cells required approximately 12 h for a revolution.

## 5. RESULTS AND DISCUSSION

**5.1. Validating Simulated Concentration through PLIF Data.** The concentration fields of the PLIF experiment and CFD simulation in the $x/d = 0$ plane at $\beta = 0°$ are illustrated in Figure 4. The progression of the simulated concentration distribution concerning the dimensionless time $tN$, denoting the rotor revolution, is discussed later in Figure 6.

To quantitatively assess the disparity between the experimental data and simulated results, concentration profiles are presented in Figure 5 along a vertical line at $z/d = 0.45$ and a horizontal line $y/d = 1.3$. Minor discrepancies are observed; for example, the peak values of PLIF are higher than those of CFD at $y/d = 1.2$ in the left panel and $z/d = 0.8$ in the right panel. In general, the concentration results of the simulation agree well with those of the experiments.

In addition, simulated concentration profiles with different grids are shown in Figure 5. As we reported in our previous work,[8] the concentration field exhibits greater sensitivity to cell spacing than the velocity field. A smaller cell size results in a more precise simulated concentration distribution. Given $Sc = 1.4 \times 10^9$ mentioned above, the distance of scalar diffusion $\delta$ over a characteristic flow time $d/V_{tip}$ can be calculated as $\delta/d = (ScRe)^{-0.5} = 2.99 \times 10^{-4}$. Consequently, to fully acquire concentration details, the total number of cells within a cavity should be on the order of $\frac{4}{3}\pi(0.5 \times d/\delta)^3 \approx 10^{10}$, a scale



https://doi.org/10.1021/acs.iecr.3c04570
Ind. Eng. Chem. Res. 2024, 63, 4164−4175

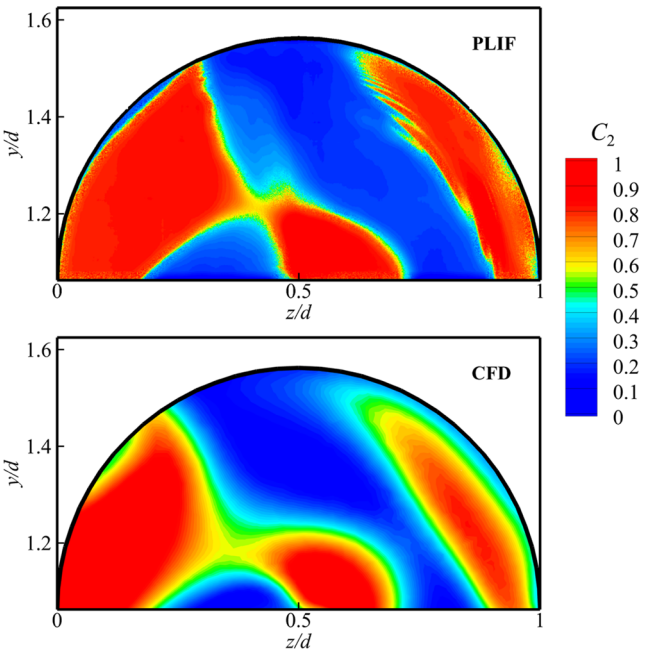


**Figure 4.** Experimental (top panel) and simulated (bottom panel) concentration fields of fluid 2 in the stator cavity at $\beta = 0°$, $Q = 80$ mL/min, $N = 1$ rev/min, and $\mu = 20$ Pa·s. The PLIF experimental results represent the mean concentration field derived from 100 frames measured at an identical angle $\beta$. On the other hand, the simulated data, based on 4 million cells, presents an instantaneous concentration field at $tN = 10$.

beyond the current computational capabilities. As illustrated in Figure 5, the simulated concentration profiles, utilizing 4 million cells, demonstrate a favorable alignment with the experimental results. Further increasing the number of cells did not lead to significant improvements, and further increasing cells did not lead to further development. Consequently, subsequent simulations were performed using 4 million cells, which is a trade-off between the accuracy and computational cost.

As shown in Figure 6, the concentration profiles were simulated with different time steps $\Delta t$ at $\beta = 0°$ and $tN = 10$. This figure shows that the profiles completely overlap along the vertical line $z/d = 0.45$ and the horizontal line $y/d = 1.3$, which confirms time-step independence. In later simulations, the time step is 0.1 s at $N = 1$ rev/min. To maintain a constant Courant−Friedrichs−Levy number (around 0.185), $\Delta t$ was varied from 0.1 to 0.025 s with the rotating speed ranging from 1 to 4 rev/min.

The instantaneous concentration profiles along the vertical and horizontal lines at different times are shown in Figure 7. The concentration profiles after 10 revolutions overlap with those after 15 revolutions; that is, the concentration field becomes steady after 10 revolutions. Thus, we previously compared the experimental results with the simulated results after a steady state was reached. Notably, given that the fluid region in the dynamic mixer periodically changes with angle $\beta$, the simulation is inherently transient. In this context, "steady" implies that the flow field at the same angle $\beta$ has reached full development.

**5.2. Flow Pattern in the Dynamic Mixer.** The simulated flow pattern of the dynamic mixer in the axial direction is shown in Figure 8. In general, the fluid moves propelled by the pressure disparity between the inlets and the outlet. During this journey from inlets to outlet, the fluid is pumped into a row of stator cavities first and then squeezed into rotor cavities, subsequently to the next row of stator cavities, and so on. Simultaneously, as the rotor revolves, transporting the fluid in the circumferential direction, the axial flow within the dynamic mixer exhibits a periodic behavior. The flow channel between the cavities of the rotor and stator varies with $\beta$, which is shown in Figure 1(c). It is noticeable that the area of the overlapping region of the fluid reaches a maximum at $\beta = 0°$.

To clearly show the dynamic process in the axial direction, Figure 9 illustrates a variety of local flow patterns within a period ($0° \leq \beta < 60°$). As a result of the combined motion caused by the pressure-driven flow and rotor rotation, the fluid undergoes a sequence of concentrations and expansions. This process involves repetitive stretching and stacking, which contributes significantly to the mixing of highly viscous fluids.

In the circumferential direction, the geometry, and consequently the flow, exhibit a periodicity of 60°. Figure 10 displays four representative flow patterns by depicting the dimensionless velocity distribution in the $z/d = 1.4$ plane over one period (a to c and f). The flow patterns within the stator and rotor cavities vary with angle $\beta$, leading to a diverse array of mechanisms in fluid transmission between cavities. To clearly depict the fluid flow between the stator and rotor cavities, the fluid velocity in the rotating region is presented as the relative velocity based on the rotor. At $\beta = 0°$, the cavities of the stator and rotor are aligned in the axial direction, and the

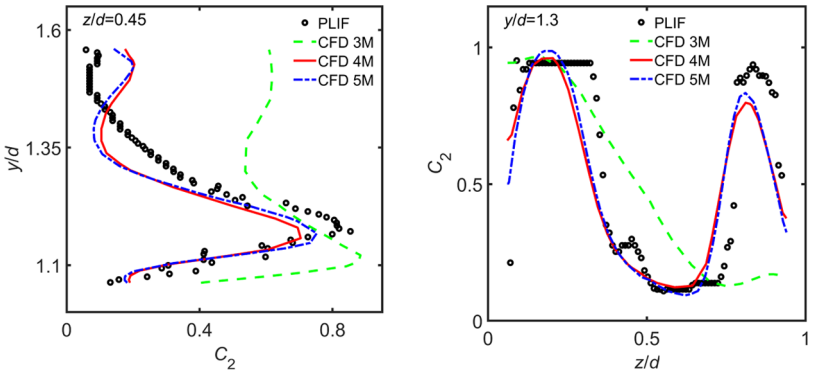


**Figure 5.** Comparison of the PLIF experimental and simulated concentration profiles of fluid 2 for a vertical line $z/d = 0.45$ and a horizontal line $y/d = 1.3$ at $\beta = 0°$, $Q = 80$ mL/min, $N = 1$ rev/min, and $\mu = 20$ Pa·s. The simulated results with 3, 4, and 5 million cells are denoted as CFD 3M, 4M, and 5M, respectively.



https://doi.org/10.1021/acs.iecr.3c04570
Ind. Eng. Chem. Res. 2024, 63, 4164−4175

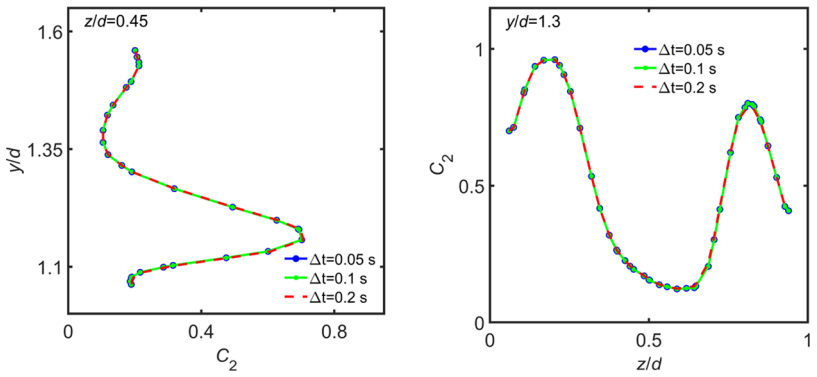


**Figure 6.** The instantaneous concentration profiles of fluid 2 with different time steps $\Delta t$ at $\beta = 0°$ and $tN = 10$ on a vertical line $z/d = 0.45$ and a horizontal line $y/d = 1.3$. Operation conditions: $Q = 80$ mL/min, $N = 1$ rev/min, and $\mu = 20$ Pa·s.

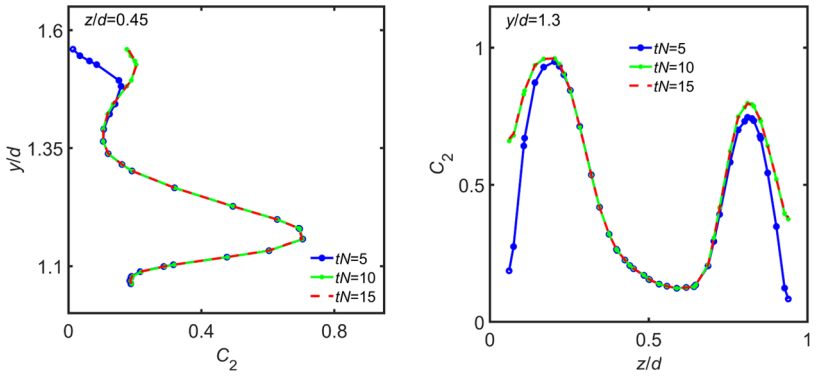


**Figure 7.** Instantaneous concentration profiles of fluid 2 at $\beta = 0°$ on a vertical line $z/d = 0.45$ and a horizontal line $y/d = 1.3$ at $tN = 5$, 10, and 15, respectively. Operation conditions: $Q = 80$ mL/min, $N = 1$ rev/min, and $\mu = 20$ Pa·s.

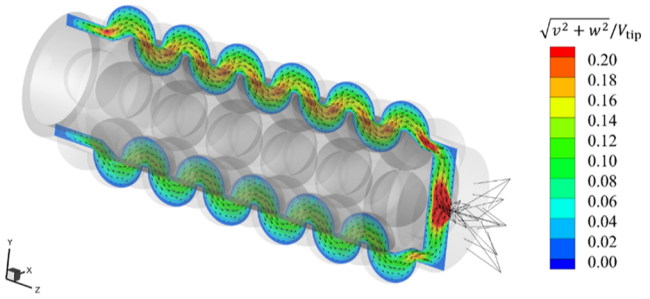


**Figure 8.** Simulated steady velocity field in the $x/d = 0$ plane at $\beta = 0°$, $Q = 80$ mL/min, $N = 1$ rev/min, and $\mu = 20$ Pa·s.

current stator cavity, indicated by a blue arrow, is not connected to the trailing stator cavity by the rotor cavity, as indicated by a red arrow. When $\beta = 15°$, the fluid circulates within both the stator and rotor cavities, propelled by the shear flow generated by the combined effects of the fluid within the cavities and the cavity walls. As the rotor rotates to $\beta = 30°$, the current rotor cavity connects to the leading stator cavity and the trailing stator cavity, and fluids obviously transfer in the circumferential direction. The vortex center of the fluid in the cavities moves toward the middle of the stator cavity, resulting in an increase in velocity. When $\beta = 45°$, the vortex center in the stator cavity keeps moving clockwise, while, in the rotor cavity, it moves in the opposite direction. Meanwhile, the connection between the stator and rotor cavities in the circumferential direction breaks down, resulting in weakening of the circulation flow.

The flow pattern also varies in the axial direction, as shown in Figure 10(d)−(f). Compared with the flow pattern at $z/d = 1.4$, the flow patterns at $z/d = 0.5$ and $z/d = 1.1$ present no overlap between the cavities of the rotor and stator at the circumferential cross sections. In the former, the circulation flow in the stator cavities is caused only by the rotor itself. In the latter, the velocity in the rotor cavities is high and decreases near the stator wall because of the boundary effect. In addition, we note here that the flow fields in each cavity are markedly different from each other in the circumferential cross sections. This is due to the feeding flow rate at inlet 1 is 4 times higher than that at inlet 2. Overall, in the circumferential cross sections, simulated flow fields show that the fluid flow experiences extension, shearing, and stacking of highly viscous fluid to promote the transfer phenomenon.

The mixing behavior is attained through the fluid flow generated in the mixer. Therefore, mixing effectiveness is related to the flow patterns in the dynamic mixer. Characterizing the flow patterns is essential for obtaining insight into the performance of the dynamic mixer.

In a mixing device, the local rate of deformation is influenced by a blend of shear, elongational, and rotational flows. The velocity gradient $\nabla \boldsymbol{V}$ can be decomposed into two parts as follows

$$\nabla \boldsymbol{V} = \underbrace{\frac{1}{2}(\nabla \boldsymbol{V} + \nabla \boldsymbol{V}^T)}_{\boldsymbol{D}} + \underbrace{\frac{1}{2}(\nabla \boldsymbol{V} - \nabla \boldsymbol{V}^T)}_{\boldsymbol{\Omega}} \tag{7}$$

The first term on the right-hand side is the strain rate tensor $\boldsymbol{D}$, and the second term is the vorticity tensor $\boldsymbol{\Omega}$.



https://doi.org/10.1021/acs.iecr.3c04570
Ind. Eng. Chem. Res. 2024, 63, 4164−4175

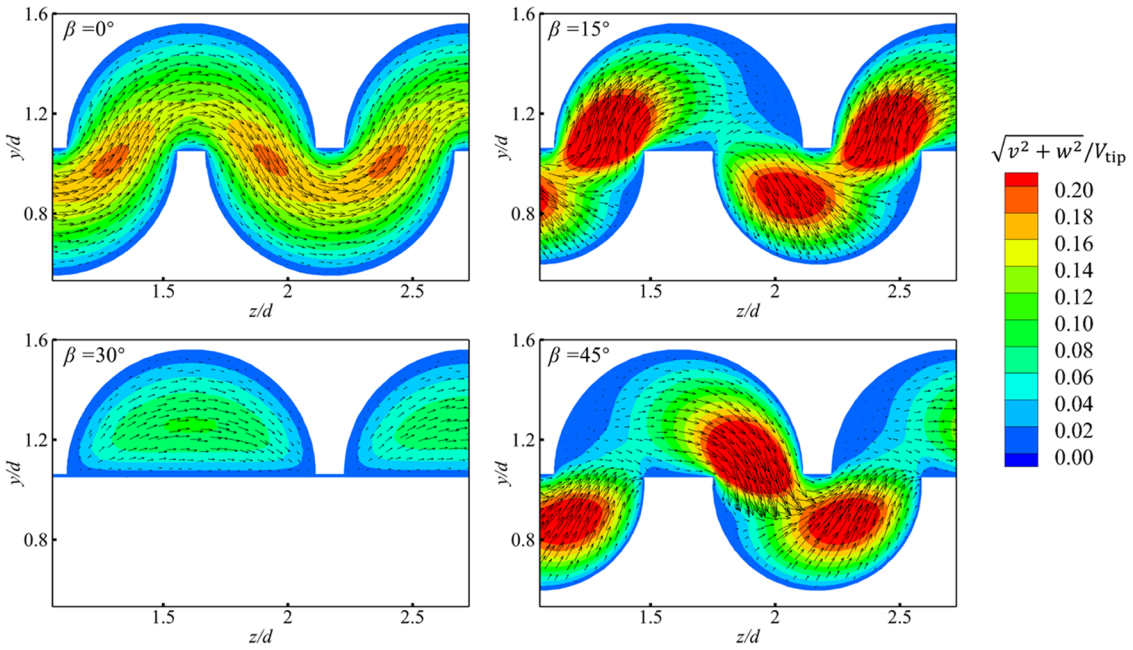


**Figure 9.** Simulated local velocity fields for different angles $\beta$ between the stator and rotor in the $x/d = 0$ plane at $Q = 80$ mL/min, $N = 1$ rev/min, and $\mu = 20$ Pa·s.

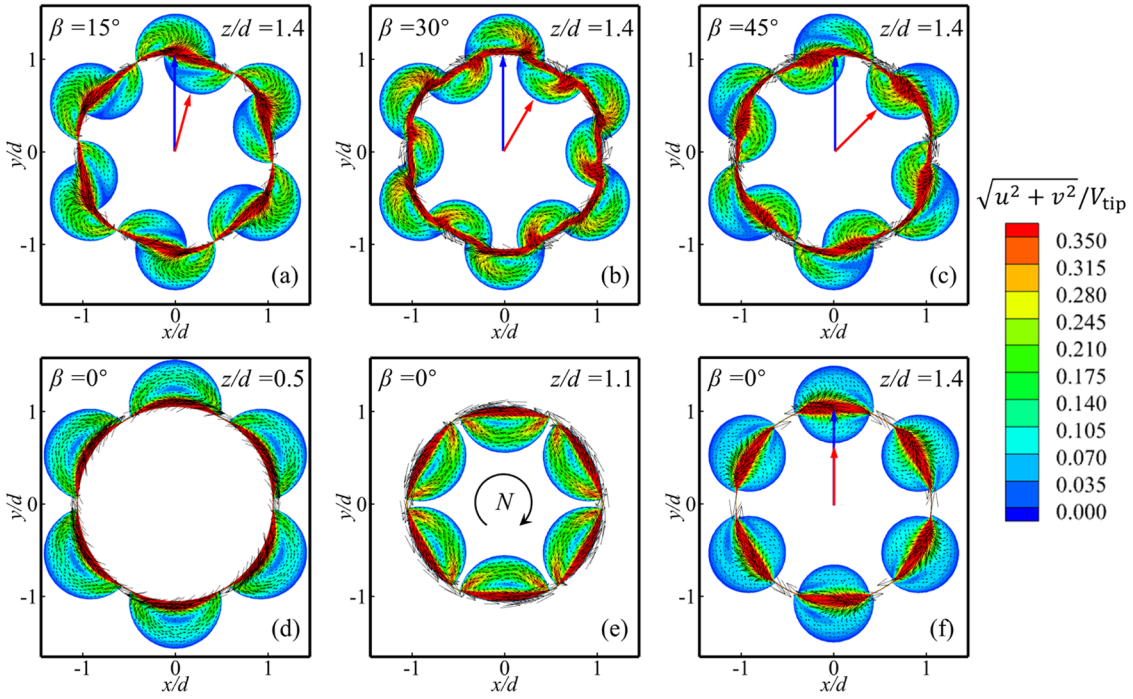


**Figure 10.** Simulated velocity fields in the stator and rotor for different angles $\beta$ and axial planes at $Q = 80$ mL/min, $N = 1$ rev/min, and $\mu = 20$ Pa·s. (a) $z/d = 1.4$, $\beta = 15°$; (b) $z/d = 1.4$, $\beta = 30°$; (c) $z/d = 1.4$, $\beta = 45°$; (d) $z/d = 0.5$, $\beta = 0°$; (e) $z/d = 1.1$, $\beta = 0°$; and (f) $z/d = 1.4$, $\beta = 0°$. The flow in the stator cavities is in a fixed reference frame, and the flow in the rotor cavities is in a reference frame rotating with the rotor. The blue arrow points toward the stator cavity, while the red arrow points toward the rotor cavity.

The effectiveness of elongational flows in laminar mixing has been widely acknowledged.[1] To quantify the level of elongational flow, the mixing index $\lambda$ is defined as[21]

$$\lambda = \frac{3\sqrt{6}\det \boldsymbol{D}}{(\boldsymbol{D}:\boldsymbol{D})^{3/2}} \tag{8}$$

$\lambda = 1$ is a uniaxial elongational flow for fluid convergence; $\lambda = -1$ is a biaxial elongational flow for fluid bifurcation; and $\lambda = 0$ is a planar shear flow. Under general conditions of $0 < |\lambda| < 1$, the flow pattern results from the superposition of both elongational and shear flows.

Figure 11 presents the distribution of $\lambda$ in the $x/d = 0$ plane along the entire length of the mixer. The fluid experiences a shearing flow as a consequence of the relative motion of the rotor and stator walls. The fluid experiences repetitive convergence and divergence between the rotor and stator



https://doi.org/10.1021/acs.iecr.3c04570
Ind. Eng. Chem. Res. 2024, 63, 4164−4175

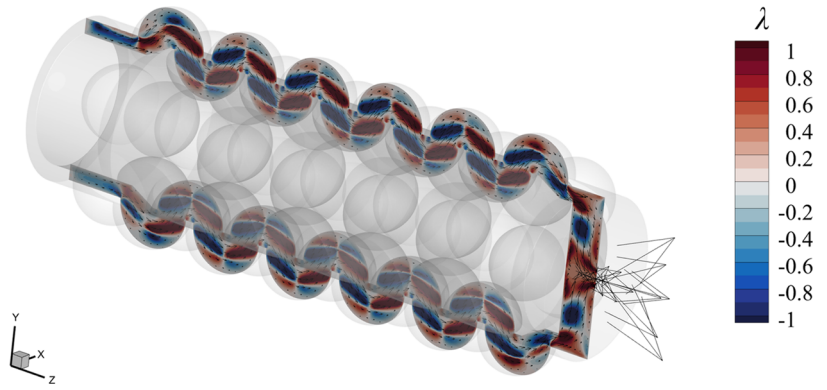


**Figure 11.** Simulated distribution of the mixing index $\lambda$ in the $x/d = 0$ plane at $\beta = 0°$, $N = 1$ rev/min, $Q = 80$ mL/min, and $\mu = 20$ Pa·s.

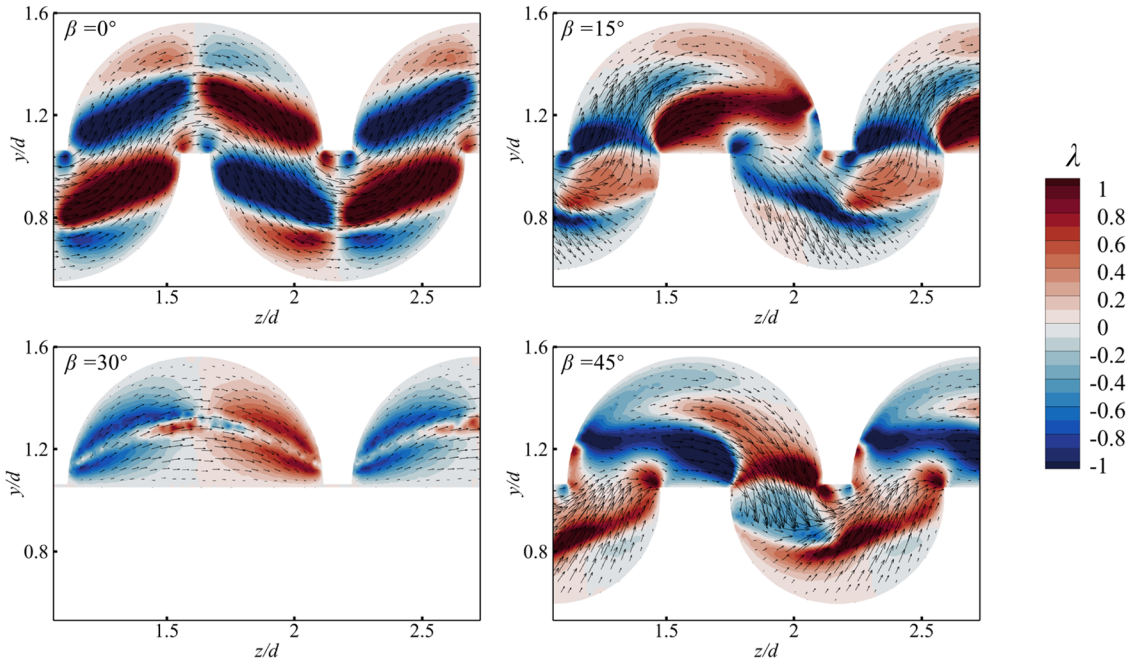


**Figure 12.** Simulated local distribution of the mixing index rate $\lambda$ for different $\beta$ angles between the stator and rotor in the $x/d = 0$ plane at $N = 1$ rev/min, $Q = 80$ mL/min, and $\mu = 20$ Pa·s.

cavities, leading to a highly elongational flow. Fluid elements move back and forth within the elongational flow region, repeatedly bifurcating and converging, thereby providing numerous opportunities for stretching and stacking. When the fluid flows in the cavity, it is divergent ($\lambda = -1$) and stacked with adjacent fluids; when the fluid flows out of the cavity, it is convergent ($\lambda = 1$) and stretched by the narrow configuration. The distribution of $\lambda$ is periodic in the axial direction, which is consistent with the periodic flow pattern. However, the contour of $\lambda$ is not symmetric along the centerline of the mixer due to asymmetric feed flow.

Figure 12 shows the local distribution of $\lambda$ for different $\beta$ angles in the $x/d = 0$ plane. Depending on $\beta$, the flow pattern along the axial direction varies, leading to diverse $\lambda$ distributions for the fluid. It can be observed clearly that the regions of $\lambda < 0$ and $\lambda > 0$ are periodic and alternating, which means fluids undergo convergence and divergence repeatedly in the elongational flow. As the cavity configuration varies with $\beta$, the region of elongational flow (strongly positive and negative $\lambda$) always coincides with the region of fluid flowing at a high velocity. This suggests that the elongational flow is the dominant flow pattern along the axial direction.

Figure 13 shows the distribution of $\lambda$ in the circumferential cross sections. Similar to the flow characteristics, the distribution of $\lambda$ varies with space and time. The distribution of $\lambda$ varies with the location and shape of the vortex in the recirculating fluid as the rotor rotates. The fluid near the walls of the stator and rotor cavities experiences a strong shear, as indicated by $\lambda$ values close to zero, while the fluid on the recirculating path undergoes stretching and stacking. It is worth noting that the region of high-velocity magnitude in Figure 10 largely overlaps with the region of the elongational flow. In other words, the main fluid flow in the dynamic mixer is predominantly an elongational flow rather than a shearing flow.

**5.3. Mixing Characteristics in the Dynamic Mixer.** To explore the influence of the operating conditions on the mixing process of highly viscous fluids within the dynamic mixer, a series of simulation cases were conducted, considering different feeding flow rates, rotating speeds, and fluid viscosities. The simulation settings are listed in Table 1.



https://doi.org/10.1021/acs.iecr.3c04570
Ind. Eng. Chem. Res. 2024, 63, 4164−4175

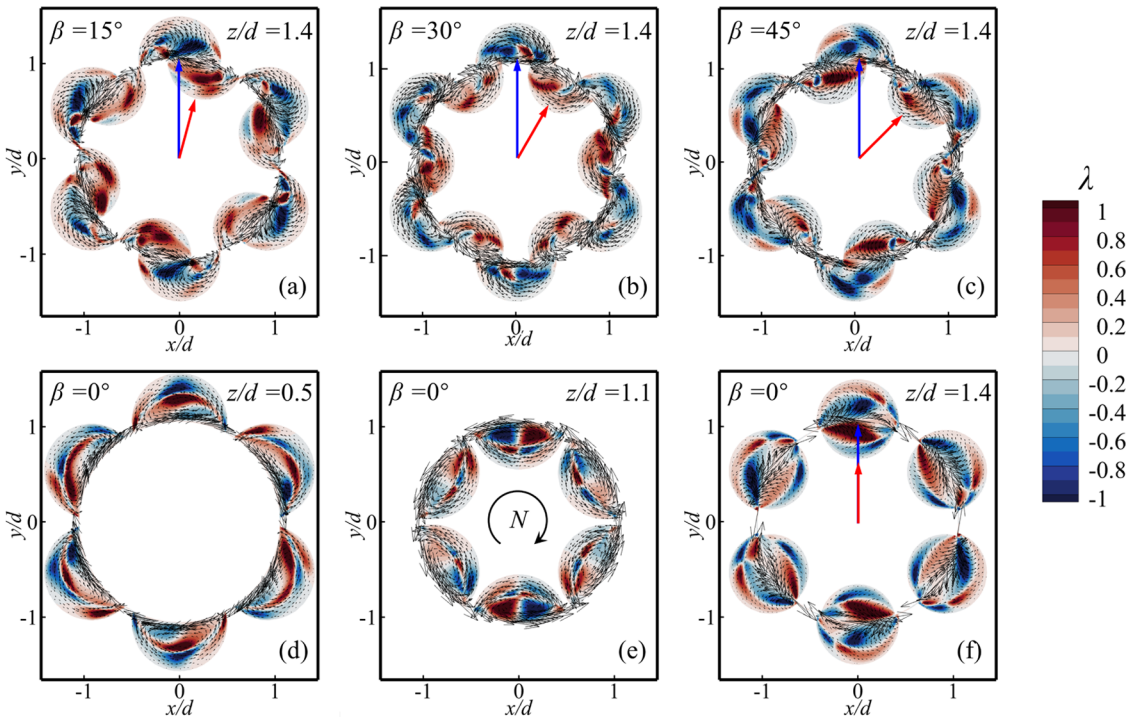


**Figure 13.** Simulated distributions of the mixing index $\lambda$ for different $\beta$ angles and axial planes at $N$ = 1 rev/min, $Q$ = 80 mL/min, and $\mu$ = 20 Pa·s. (a) $z/d$ = 1.4, $\beta$ = 15°; (b) $z/d$ = 1.4, $\beta$ = 30°; (c) $z/d$ = 1.4, $\beta$ = 45°; (d) $z/d$ = 0.5, $\beta$ = 0°; (e) $z/d$ = 1.1, $\beta$ = 0°; and (f) $z/d$ = 1.4, $\beta$ = 0°.

**Table 1. Numerical Simulation Settings**

| case | $N$ (rev/min) | $V_{tip}$ (m/s) | $Q$ (mL/min) | $\rho$ (kg/m3) | $\mu$ (Pa·s) | $M_1$ (wt %) |
|---|---|---|---|---|---|---|
| 1 | 1 | $1.85 \times 10^{-3}$ | 320 | 1386 | 20 | 80 |
| 2 | 1 | $1.85 \times 10^{-3}$ | 480 | 1386 | 20 | 80 |
| 3 | 1 | $1.85 \times 10^{-3}$ | 640 | 1386 | 20 | 80 |
| 4 | 2 | $8.80 \times 10^{-3}$ | 640 | 1386 | 20 | 80 |
| 5 | 4 | $1.76 \times 10^{-2}$ | 640 | 1386 | 20 | 80 |
| 6 | 1 | $1.85 \times 10^{-3}$ | 640 | 1386 | 60 | 80 |
| 7 | 1 | $1.85 \times 10^{-3}$ | 640 | 1386 | 100 | 80 |

The quantitative description of mixing efficiency is characterized by the coefficient of variation (COV) within sections of the dynamic mixer[22]

$$\mathrm{COV} = \frac{\sigma}{\overline{C}} \tag{9}$$

$$\sigma = \sqrt{\frac{\iint_A (\overline{C} - C_i)^2 \, dA}{A}} \tag{10}$$

$$\overline{C} = \frac{\iint_A C_i \, dA}{A} \tag{11}$$

where $\sigma$ is the standard deviation, $\overline{C}$ represents the average concentration over a chosen section, and $A$ is the area of the section ($m^2$). The smaller the COV, the more uniform the concentration field.

To investigate the relationship between the flow pattern and mixing characteristics, the absolute values of the mixing index $|\lambda|$ under different operating conditions were also calculated. The value of $|\lambda|$ is zero for planar shear, unity for pure elongational flow, and $0 < |\lambda| < 1$ for situations in between

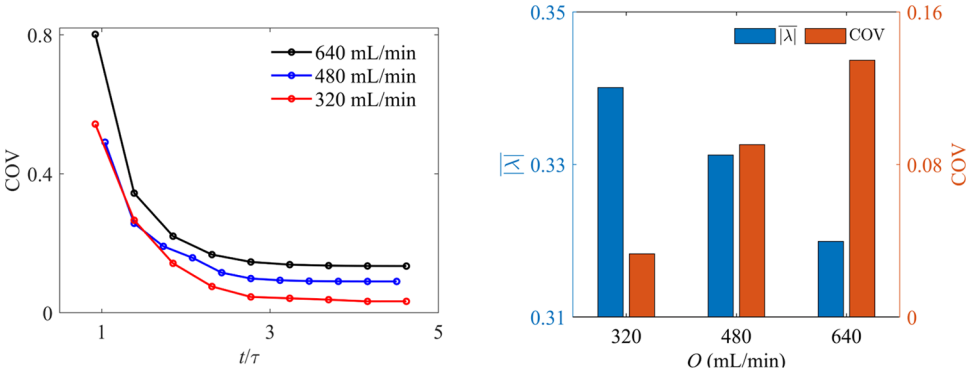


**Figure 14.** Left panel: instantaneous COV of fluid 2 in the outlet plane at three feeding flow rates, $Q$. Right panel: the volume-averaged $|\lambda|$ and COV of fluid 2 in the outlet plane at three feeding flow rates with $t/\tau$ = 4.5. The operating conditions for the two panels are $N$ = 1 rev/min and $\mu$ = 20 Pa·s.



https://doi.org/10.1021/acs.iecr.3c04570
Ind. Eng. Chem. Res. 2024, 63, 4164−4175

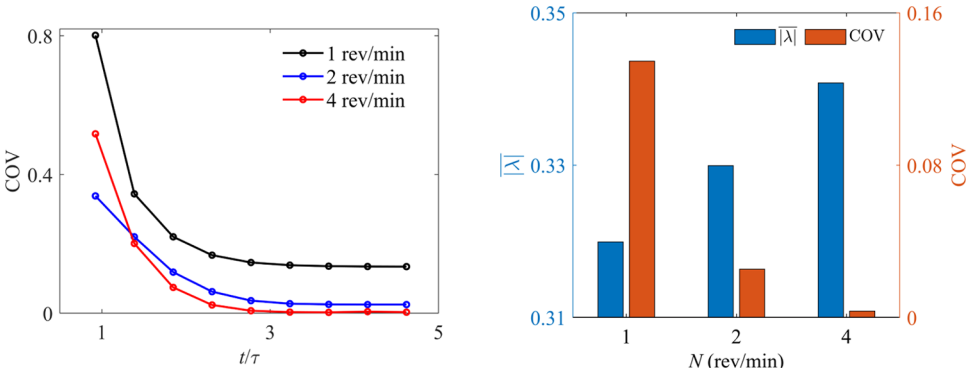


**Figure 15.** Left panel: instantaneous COV of fluid 2 in the outlet plane at three rotor rotating speeds, $N$. Right panel: the volume-averaged $|\lambda|$ and COV of fluid 2 in the outlet plane at three rotor rotating speeds with $t/\tau = 4.5$. The operating conditions for the two panels are $Q = 640$ mL/min and $\mu = 20$ Pa·s.

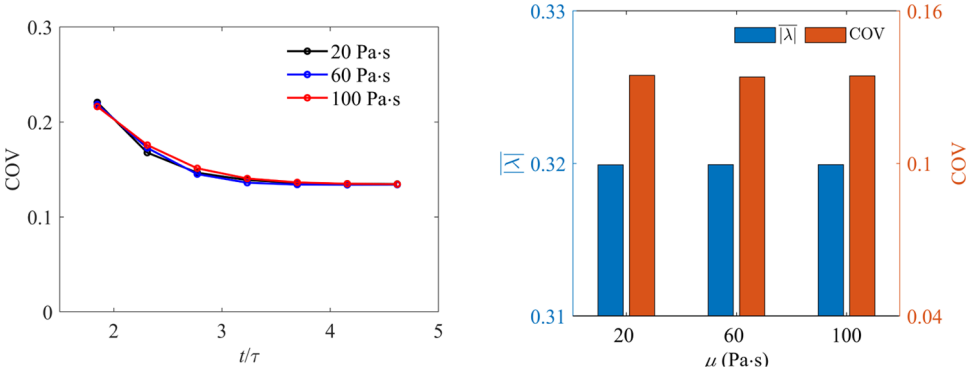


**Figure 16.** Left panel: instantaneous COV of fluid 2 in the outlet plane at three fluid viscosities, $\mu$. Right panel: the volume-averaged $|\lambda|$ and COV of fluid 2 in the outlet plane at three fluid viscosities with $t/\tau = 4.5$. The operating conditions for the two panels are $Q = 640$ mL/min and $N = 1$ rev/min.

these two extremes. The volume-averaged $|\lambda|$ can be calculated by the following equation

$$\overline{|\lambda|} = \frac{\iiint_V |\lambda_i| dV}{V} \tag{12}$$

where $\overline{|\lambda|}$ is the volume-averaged $|\lambda|$ in the dynamic mixer, and $V$ is the fluid volume of the dynamic mixer.

The time is normalized by the mean residence time $\tau$ of the dynamic mixer, yielding the dimensionless time

$$\frac{t}{\tau} = \frac{t}{V/Q} \tag{13}$$

where $Q$ is the sum of the flow rates at the two inlets.

*5.3.1. Effect of Feeding Flow Rate on Mixing Performance.* As shown in the left panel of Figure 14, the mixing performance of the highly viscous fluids improves with decreasing feeding flow rate in the dynamic mixer. Additionally, the COV curve for higher feeding flow rates stabilizes more rapidly.

To investigate the influence of the feeding flow rate on the mixing process, both the volume-averaged $|\lambda|$ and instantaneous COV, after the mixing became steady, are depicted in the right panel of Figure 14. With an increase in the flow rate, there is a decrease in the volume-averaged $|\lambda|$, and simultaneously, the COV increases. This suggests that as the flow rate increases, a larger portion of the dynamic mixer is dominated by the shearing flow, which exhibits a lower mixing efficiency compared to the elongational flow.

*5.3.2. Effect of Rotor Rotating Speed on Mixing Performance.* The influence of the rotor rotating speed on the mixing process in the dynamic mixer is shown in the left panel of Figure 15. At the end of the curves, it is evident that the COV value decreases with an increase in the rotor rotating speed, indicating an increase in the mixing performance.

In the right panel of Figure 15, the volume-averaged $|\lambda|$ and COV values at the outlet became stable. At a higher rotating speed, the highly viscous fluids experience a stronger elongational flow, resulting in a lower COV value at the same time. Undoubtedly, higher rotating speeds result in stronger shear near the rotor−stator interface. If we assume that the elongational flow remains constant, according to the definition of $|\lambda|$, it should decrease with increasing rotating speed. However, in Figure 15, $|\lambda|$ increases with the rotating speed, suggesting that the increase in the degree of elongational flow is greater than that of shear flow. In other words, the flow pattern associated with a higher rotating speed enhances the mixing process in the dynamic mixer.

*5.3.3. Effect of Fluid Viscosity on Mixing Performance.* The left panel of Figure 16 demonstrates the influence of fluid viscosity on the mixing performance. The COV values for cases with different fluid viscosities show slight differences in the early stages of the mixing process. As time progresses, the COV values become very close, confirming that the mixing of highly viscous fluids in this system is not dependent on viscosity. This finding is consistent with our previous observation in a lid-driven cavity.[23]



https://doi.org/10.1021/acs.iecr.3c04570
Ind. Eng. Chem. Res. 2024, 63, 4164−4175

Furthermore, the right panel of Figure 16 compares the flow patterns of the cases with different fluid viscosities with respect to mixing performance. Interestingly, the volume-averaged $|\lambda|$ is almost unaffected by fluid viscosity, indicating that the flow pattern of the highly viscous fluid in the dynamic mixer is not sensitive to changes in viscosity. Based on these findings, we can infer that the similarity in the mixing performance is due to the similar flow motions of the fluids.

## 6. CONCLUSIONS

The flow patterns and mixing performance in a dynamic mixer were assessed through a combination of PLIF experiments and CFD simulations. To obtain the concentration field of the dynamic mixer, a refractive index-matched technique was used in the experiment, which has not been previously reported for such a system. The experimental system was carefully calibrated, and the measured concentration field provided a valuable set of data for validating numerical models and methods.

In general, the simulated results align well with the experimental data, and any discrepancies between them are thoroughly discussed. The simulated flow patterns illustrate that the fluids experienced extension, shearing, and stacking processes, promoting transfer phenomena in the dynamic mixer. The mixing index $\lambda$ was used for evaluating the proportions of elongational and shear flows. Due to the spatially symmetric geometry of the dynamic mixer, the flow field and $\lambda$ distribution showed axial and circumferential periodicity.

Then, an experimentally validated simulation method was applied to investigate the mixing process under different conditions in terms of the coefficient of variation (COV) as a function of time. For highly viscous fluids, the mixing performance improved with a lower feeding flow rate and a higher rotating speed. It is interesting that viscosity itself plays a marginal role in the mixing of highly viscous fluids. However, once the Reynolds number is well below 1, the flow becomes Re-independent, and since Sc is very large, numerical diffusion will not differ much between cases with different viscosities. The relationship between the flow pattern and mixing characteristics was also considered quantitatively. After the mixing performance state achieved time independence, the simulations consistently showed that an improvement in mixing (i.e., a reduction of COV) was associated with a slight increase of the volume-averaged $|\lambda|$. This suggests that elongational flow is more effective than shear flow in promoting the mixing of highly viscous fluids. These results can guide dynamic mixer design and assist in optimization in the development of high-performance polymers.

## AUTHOR INFORMATION


### Corresponding Authors

**Zhipeng Li** − *State Key Laboratory of Chemical Resource Engineering, School of Chemical Engineering, Beijing University of Chemical Technology, Beijing 100029, China;* orcid.org/0000-0003-1450-8836; Email: lizp@mail.buct.edu.cn

**Zhengming Gao** − *State Key Laboratory of Chemical Resource Engineering, School of Chemical Engineering, Beijing University of Chemical Technology, Beijing 100029, China;* Email: gaozm@mail.buct.edu.cn

### Authors

**Junhao Wang** − *State Key Laboratory of Chemical Resource Engineering, School of Chemical Engineering, Beijing University of Chemical Technology, Beijing 100029, China;* orcid.org/0009-0006-7889-6400

**J. J. Derksen** − *School of Engineering, University of Aberdeen, Aberdeen AB24 3UE, U.K.;* orcid.org/0000-0002-9813-356X

Complete contact information is available at: https://pubs.acs.org/10.1021/acs.iecr.3c04570


### Notes

The authors declare no competing financial interest.

## ACKNOWLEDGMENTS

The authors gratefully acknowledge financial support from the National Natural Science Foundation of China (No. 22178014), which was essential for the success of this research project.

## NOMENCLATURE

| | |
|---|---|
| $A$ | area of the section [$m^2$] |
| $C$ | concentration (mass fraction) [−] |
| $\boldsymbol{D}$ | strain rate tensor [1/s] |
| $D$ | diffusion coefficient [$m^2$/s] |
| $D_{rotor}$ | diameter of the rotor [m] |
| $D_{stator}$ | diameter of the stator [m] |
| $d$ | diameter of the cavities [m] |
| $F$ | fluorescence intensity [cd] |
| $g$ | gravitational acceleration vector [$m/s^2$] |
| $I$ | excitation intensity [cd] |
| $N$ | rotating speed [rev/min] |
| $n$ | refractive index [−] |
| $p$ | pressure [Pa] |
| $Q$ | volumetric flow rate [mL/min] |
| $t$ | time [s] |
| $uvw$ | velocity magnitude in $x$, $y$, and $z$ directions [m/s] |
| $\boldsymbol{V}$ | vector of velocity [m/s] |
| $V_{tip}$ | tip speed of the rotor [m/s] |
| $xyz$ | cartesian coordinates [m] |

## GREEK LETTERS

| | |
|---|---|
| $\beta$ | angle between the rotor and stator [deg] |
| $\Delta t$ | time step in simulation [s] |
| $\delta$ | scalar diffusion distance [m] |
| $\lambda$ | mixing index [−] |
| $\mu$ | viscosity of fluids [Pa·s] |
| $\rho$ | density of fluids [$kg/m^3$] |
| $\sigma$ | standard deviation [−] |
| $\tau$ | space time [s] |
| $\boldsymbol{\Omega}$ | vorticity tensor [1/s] |

## REFERENCES


(1) Todd, D. B. Mixing of Highly Viscous Fluids, Polymers, and Pastes. In *Handbook of Industrial Mixing*; John Wiley & Sons, Ltd, 2003; pp 987−1025.

(2) Ottino, J. M.; Chella, R. Laminar Mixing of Polymeric Liquids; a Brief Review and Recent Theoretical Developments. *Polym. Eng. Sci.* **1983**, *23* (7), 357−379.

(3) Alvarez, M. M.; Zalc, J. M.; Shinbrot, T.; Arratia, P. E.; Muzzio, F. J. Mechanisms of Mixing and Creation of Structure in Laminar Stirred Tanks. *AIChE J.* **2002**, *48* (10), 2135−2148.

(4) Kolomiets, A.; Jirout, T. Analysis of the Dispersion of Viscoelastic Clusters in the Industrial Rotor-Stator Equipment. *Processes* **2021**, *9* (12), 2232.
(5) Hindmarch, R. S. The Cavity Transfer Mixer: A Blender for All Seasonings. *Mater. Des.* **1987**, *8* (6), 331−339.
(6) Wang, C.; Manas-Zloczower, I. Flow Field Analysis of a Cavity Transfer Mixer. *Polym. Eng. Sci.* **1994**, *34* (15), 1224−1230.
(7) Grosso, G.; Hulsen, M. A.; Sarhangi Fard, A.; Overend, A.; Anderson, P. D. Mixing Processes in the Cavity Transfer Mixer: A Thorough Study. *AIChE J.* **2018**, *64* (3), 1034−1048.
(8) Huang, F.; Chen, P.; Wang, J.; Li, Z.; Gao, Z.; Derksen, J. J. Refractive Index-Matched PIV Experiments and CFD Simulations of Mixing in a Complex Dynamic Geometry. *Ind. Eng. Chem. Res.* **2020**, *59* (16), 7982−7992.
(9) Jaffer, S. A.; Bravo, V. L.; Wood, P. E.; Hrymak, A. N.; Wright, J. D. Experimental Validation of Numerical Simulations of the Kneading Disc Section in a Twin Screw Extruder. *Polym. Eng. Sci.* **2000**, *40* (4), 892−901.
(10) Cortada-Garcia, M.; Weheliye, W. H.; Dore, V.; Mazzei, L.; Angeli, P. Computational Fluid Dynamic Studies of Mixers for Highly Viscous Shear Thinning Fluids and PIV Validation. *Chem. Eng. Sci.* **2018**, *179*, 133−149.
(11) Alberini, F.; Simmons, M. J. H.; Ingram, A.; Stitt, E. H. Use of an Areal Distribution of Mixing Intensity to Describe Blending of Non-Newtonian Fluids in a Kenics KM Static Mixer Using PLIF. *AIChE J.* **2014**, *60* (1), 332−342.
(12) Ikarashi, Y.; Fujisawa, N. Mass Transfer Measurements and Flow Separation Behavior in a 90° Short Elbow. *Int. J. Heat Mass Transfer* **2019**, *136*, 1106−1114.
(13) Yuki, K.; Hasegawa, S.; Sato, T.; Hashizume, H.; Aizawa, K.; Yamano, H. Matched Refractive-Index PIV Visualization of Complex Flow Structure in a Three-Dimentionally Connected Dual Elbow. *Nucl. Eng. Des.* **2011**, *241* (11), 4544−4550.
(14) Zhu, L.; Cai, T.; Huang, J.; Stringfellow, T. C.; Wall, M.; Yu, L. Water Self-Diffusion in Glassy and Liquid Maltose Measured by Raman Microscopy and NMR. *J. Phys. Chem. B* **2011**, *115* (19), 5849−5855.
(15) Arbeloa, I. L.; Rohatgi-Mukherjee, K. K. Solvent Effect on Photophysics of the Molecular Forms of Rhodamine B. Solvation Models and Spectroscopic Parameters. *Chem. Phys. Lett.* **1986**, *128* (5), 474−479.
(16) Crimaldi, J. P. Planar Laser Induced Fluorescence in Aqueous Flows. *Exp. Fluids* **2008**, *44* (6), 851−863.
(17) Irani, R. R.; Adamson, A. W. Transport Processes in Binary Liquid Systems. *J. Phys. Chem. A* **1958**, *62* (12), 1517−1521.
(18) Hadžić, I.; Hennig, J.; Perić, M.; Xing-Kaeding, Y. Computation of Flow-Induced Motion of Floating Bodies. *Appl. Math. Modell.* **2005**, *29* (12), 1196−1210.
(19) Hamidipour, M.; Chen, J.; Larachi, F. CFD Study and Experimental Validation of Trickle Bed Hydrodynamics under Gas, Liquid and Gas/Liquid Alternating Cyclic Operations. *Chem. Eng. Sci.* **2013**, *89*, 158−170.
(20) Ferziger, J. H.; Perić, M.; Street, R. L. Finite Vol. Methods. In *Computational Methods for Fluid Dynamics*; Springer: Switzerland, 2020; pp 81−110.
(21) Nakayama, Y.; Kajiwara, T.; Masaki, T. Strain Mode of General Flow: Characterization and Implications for Flow Pattern Structures. *AIChE J.* **2016**, *62* (7), 2563−2569.
(22) Mandal, M. M.; Aggarwal, P.; Nigam, K. D. P. Liquid−Liquid Mixing in Coiled Flow Inverter. *Ind. Eng. Chem. Res.* **2011**, *50* (23), 13230−13235.
(23) Wang, J.; Ma, S.; Chen, P.; Li, Z.; Gao, Z.; Derksen, J. J. Mixing of Miscible Shear-Thinning Fluids in a Lid-Driven Cavity. *Chin. J. Chem. Eng.* **2023**, *58*, 112−123.



https://doi.org/10.1021/acs.iecr.3c04570
*Ind. Eng. Chem. Res.* 2024, 63, 4164−4175